This is an *Accepted Manuscript*, which has been through the Royal Society of Chemistry peer review process and has been accepted for publication.

Accepted Manuscripts are published online shortly after acceptance, before technical editing, formatting and proof reading. Using this free service, authors can make their results available to the community, in citable form, before we publish the edited article. We will replace this *Accepted Manuscript* with the edited and formatted *Advance Article* as soon as it is available.

You can find more information about *Accepted Manuscripts* in the **Information for Authors**.

Please note that technical editing may introduce minor changes to the text and/or graphics, which may alter content. The journal's standard **Terms & Conditions** and the **Ethical guidelines** still apply. In no event shall the Royal Society of Chemistry be held responsible for any errors or omissions in this *Accepted Manuscript* or any consequences arising from the use of any information it contains.
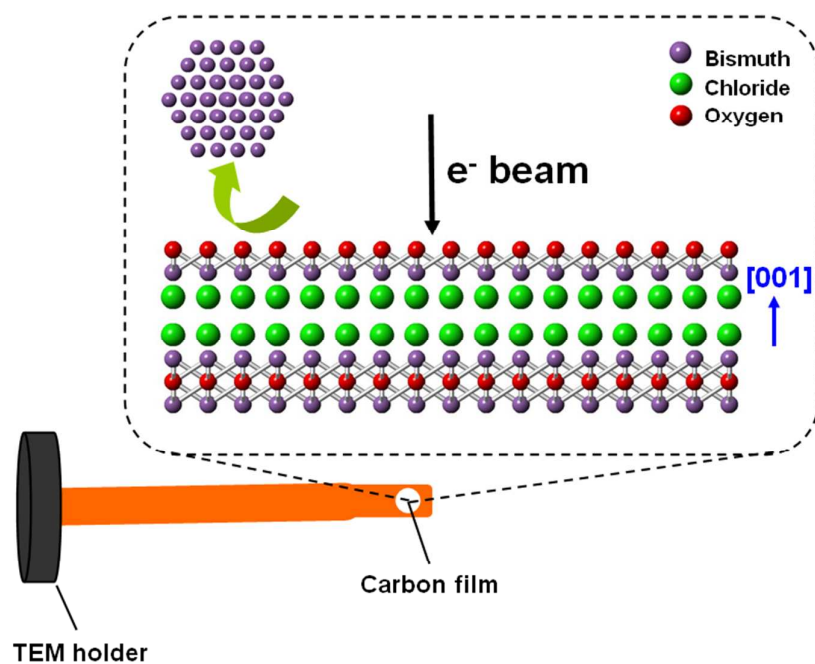
The formation and growth of bismuth nanoparticles onto BiOCl have been directly observed and characterized in a transmission electron microscope.

Journal Name

Insights into the growth of bismuth nanoparticles on 2D structured BiOCl photocatalyst: An in situ TEM investigation†

Xiaofeng Chang,[a, ‡] Shuangbao Wang,[a, ‡] Qi Qi,[b, ‡] M.A. Gondal,[c] S.G. Rashid,[c] Si Gao,[a] Deyuan Yang,[d] Kai Shen,[d] Qingyu Xu,[e] and Peng Wang[a,*]

The synthetic techniques for novel photocatalytic crystals had evolved by a trial-and-error process that spanned more than two decades, and an insight into the photocatalytic crystal growth process is a challenging area and prerequisite for achieving an excellent photoactivity. Bismuth nanoparticles based hybrids, such as Bi/BiOCl composite, have recently been investigated as highly efficient photocatalytic systems because of the localized surface plasmon resonance (LSPR) of nanostructured bismuth. In this work, the observation towards the formation and growth of bismuth nanoparticles onto 2D structured BiOCl photocatalyst has been performed in a transmission electron microscope (TEM) directly in real time. The growth of bismuth nanoparticles on BiOCl nanosheets can be emulated and speeded up driven by electron beam (e⁻ beam) in TEM. The crystallinity, growth and the elemental evolution during the formation of bismuth nanoparticles have also been probed in this work.

Introduction

Ever since the ground breaking achievement of Fujishima and Honda in 1972, TiO_2 has extensively been adopted as a promising photocatalyst for the water splitting and environmental remediation.[1-3] The quest for synthesis of alternative photocatalysts has currently attracted intense research and development in this direction because the large band gap of TiO_2 (3.2 eV for anatase and 3.0 eV for rutile) restricts the efficient harvesting of solar visible light, which is around 42 % of the total light spectrum of the solar radiations.[4] Pioneer achievements in the development of alternative photocatalysts are persistently inspiring researchers to hunt novel materials having extraordinary photocatalytic activity under visible light irradiation.[5-10] One of the designing strategies for visible light harvesting is to utilize the localized surface plasmon resonance (LSPR) of metallic nanoparticles, which can be induced by exciting surface plasmon with photons of appropriate wavelengths.[11-15] In the pool of metallic nanostructures with LSPR effect, bismuth is particularly interesting in its LSPR properties. The dependence of tunability of surface plasmon resonance band from ultraviolet to infrared on size and shape of metal particles was also revealed in both theoretical calculations and experimental studies.[16-19]

Inspired by the LSPR effect of nanostructured bismuth, various bismuth/bismuth-containing-semiconductor (Bi/BCS) hybrid systems

a. National Laboratory of Solid State Microstructures, College of Engineering and Applied Sciences and Collaborative Innovation Center of Advanced Microstructures, Nanjing University, Nanjing 210093, China;
E-mail: wangpeng@nju.edu.cn
b. School of Chemistry and Chemical Engineering, Southeast University, Nanjing 211189, China;
c. Physics Department and Centre of Excellence in Nanotechnology, King Fahd University of Petroleum and Minerals, Dhahran 31261, Saudi Arabia;
d. College of Materials Science and Technology, Nanjing University of Aeronautics and Astronautics, Nanjing 211100, China;
e. Department of Physics, Southeast University, Nanjing 211189, China.
† Electronic Supplementary Information (ESI) available: See DOI: 10.1039/x0xx00000x

have recently been synthesized and demonstrated as superior photoactive materials compared to alone BSC, and it is due to the heterojunction-like contact between bismuth nanoparticles and BCS that promotes the harvesting of visible light and efficient separation of photogenerated carries in these hybrid systems. A few routes of "one-pot" synthesis were also reported for the preparation of Bi/BCS composites using bismuth containing salts and reductants as the precursor materials, such as $Bi/(BiO)_2CO_3$ and Bi/BiOX (X=Cl, Br, I), etc.[20-22] Moreover, noticing the relatively low ionization potential of BCS crystals, progress has also been made to develop the in situ growth strategy for the synthesis of Bi/BCS heterostructured photocatalysts by partially reducing BCS into bismuth nanoparticles with the assistance of reducing matters, either by reductants or by photogenerated electrons. Weng et al. reported an in situ preparation of Bi/BiOCl heterostructured photocatalyst by reducing BiOCl in aqueous solution with the assistance of UV light irradiation and hole scavenger, and during the UV irradiation, photogenerated electrons in BiOCl semiconductor (E_g=3.4 eV) participated in the reduction of Bi(III) to form bismuth particles on the surface of BiOCl.[23] Hu et al. prepared Bi/BiOCl heterojunction photocatalysts via an in situ chemical reduction of BiOCl nanosheets in KBH_4 solution at room temperature. The combination ratio of Bi to BiOCl can be adjusted by simply changing the concentration of the reductant (KBH_4).[24] From the prospective of electrochemistry, the Zhang et al.'s report demonstrated that the BiOCl compounds at potential less than -1.16 V (vs. SHE) can be completely converted into nanostructured bismuth.[25]

The formation and possible growth dynamics, which are highly beneficial to heterogeneous nanoparticles photocatalysis, are still not very clear to date. The visualization of the crystals during growth process is fundamentally limited in conventional characterization techniques due to the fact that the results could only be obtained from the final structure. However, the technical advances in in situ electron microscopy, which has made it possible to visualize the nanocrystals growth of a step-by-step nanoscaled evolution in real time, can provide not only quantitative measurements but also

deeper insight into the growth process.[26-30] Given today's intense interests in nanomaterial and nanotechnology, it is particularly worth mentioning that the recent development of liquid cells for TEM has unprecedentedly achieved the direct observation of nanoparticle growth in a liquid solution.[31-33]

In the current investigation, we report the in situ observation of the formation and growth of bismuth nanoparticles on 2D structured BiOCl photocatalyst under a field emission gun transmission electron microscope (FEG-TEM). The electron beam (e⁻ beam) generated by 200kV FEG was used as an alternative reducing agent. Hence, the direct and real-time analysis of the formation and growth of bismuth nanoparticles was achieved easily that facilitates the in-depth understanding of the formation and growth of photocatalytic nanocrystals.

Experimental

Materials and preparation

All chemicals used in the study were of reagent grade and applied without further purification. Sodium bismuthate hydrate $(NaBiO_3 \cdot 2H_2O)$ and hydrochloric acid (HCl, 37wt %) were used as reagents supplied by Sinopharm Chemical Reagent Co., Ltd. China. Deionized (DI) water was used in the whole experiment. Single crystalline BiOCl photocatalytic crystals dominated with {001} facets were prepared for in situ TEM characterization.[34]

In addition, Bi/BiOCl-t (t=2 and 7 min) composite photocatalysts prepared at different Bi-growing stages were obtained via a UV-induced photoreduction process. Typically, 50 mg of BiOCl was added into 50 mL potassium iodide aqueous solution (KI, purchased from Sinopharm Chemical Reagent Co., Ltd. China) with concentration of 1g L^{-1}. The suspension was irradiated by a full-arc Xenon lamp (Beijing Trusttech Co., Ltd., CHF-XM) for different exposure times of "t" minutes. The resulting solid products were washed by DI water and absolute ethanol, and then dried in vacuum at 30 ^{o}C.

Characterization and optical properties

2D structured BiOCl photocatalyst was dispersed in acetone via ultrasonic treatment first, and then drop cast onto a formvar/carbon-coated copper grid or pure formvar film. TEM analysis was conducted on a FEI Tecnai F20 TEM with a field emission gun. All imaging results were obtained with an accelerating voltage of 200 kV unless otherwise specified. A Gatan Orius SC200D CCD camera was employed for in situ TEM imaging with low magnification and selected area electron diffraction (SAED). High resolution TEM images (HRTEM) were recorded with a Gatan Orius SC1000B CCD camera. High angle annular dark field imaging of scanning transmission electron microscopy (STEM-HAADF) was achieved by using a HAADF detector (Fishione, MODEL 3000) with an inner semi-angle of 36 mrad and an outer semi-angle of 180 mrad. Elemental composition was investigated by energy-dispersive X-ray spectroscopy (EDS) silicon (lithium) semiconductor drift detector.

To evaluate the capability of visible light harvesting for the composite of bismuth and BiOCl, UV-Vis absorption spectra of as-

prepared Bi/BiOCl composite photocatalysts were measured on a Varian Cary 50 UV-Vis-NIR spectrophotometer in diffuse reflectance spectrum (DRS) mode, and pure $BaSO_4$ was employed as a reference.

First-principles calculation

All ab initio calculations presented in this work were performed by employing the Cambridge Serial Total Energy Package (CASTEP) code with the Vanderbilt-type ultrasoft pseudopotentials.[35-37] The exchange-correlation functional within the generalized gradient approximation (GGA) of the Perdew-Burke-Ernzerhof (PBE) was used to solve the Kohn-Sham equations with an energy cut-off of 340 eV.[38,39] A Monkhorst-Pack grid of 6×6×3 was employed to sample the Brillouin zone.[40] The basis set of valence electronic states was set to be $6s^2 6p^3$ for bismuth, $2s^2 2p^4$ for oxygen and $3s^2 3p^5$ for chloride, respectively. Structure parameters were fully relaxed using the BFGS minimization method, in which free movement of the atoms in any direction is allowed and no symmetry constraint is imposed.[41] In self-consistent field (SCF) calculation, the Pulay density method was used, in which the convergence test was set to be 10^{-6} eV every atom.[42] In the total energy convergence test, the successive energy change on each atom was less than 1.0×10^{-5} eV, meanwhile the maximum force tolerance and total stresses were below 0.01 eV/Å and 0.05 eV/Å^3, respectively.

Results and discussion,

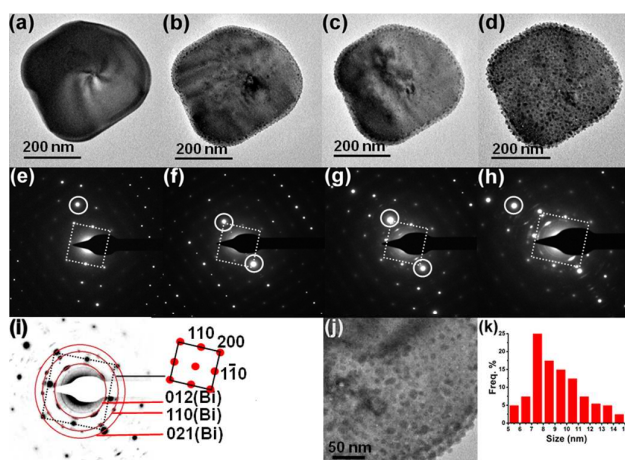### E⁻ beam dose dependence of the BiOCl crystallographic structure

Fig. 1. Low-mag TEM images and the corresponding SAED patterns of an as-prepared BiOCl nanosheet obtained under total electron irradiation dose of 8.2 ×10³ e/nm² (a, e), 2.98×10⁷ e/nm² (b, f), 5.92×10⁷ e/nm² (c, g) and 1.3×10⁸ e/nm² (d, h, i, j), respectively. (i) depicts the enlarged SAED with pattern indexation. (j) and (k) show a magnified TEM image and the corresponding size distribution histogram of bismuth nanoparticles induced by e⁻ beam irradiation, respectively. The squares and circles in (e-h) indicate the tetragonal structure of the BiOCl matrix and the changing of the brightest diffraction spots excited by the electron beam, respectively.

Fig. 1(a) and (e) show a TEM image of a representative piece of BiOCl nanosheets having size of ca. 300 nm and the corresponding selected area electron diffraction (SAED) pattern, respectively. The SAED result indicates that the nanosheet is a single crystal with tetragonal structure and closely orientated to <001> zone axis labelled with a red square. Blank experiments suggested that at low e$^-$ beam dose rate, ca 1,000 e/nm^2 ·s, no apparent changes within the nanosheets can be observed in both the TEM images and the SAEDs for 30mins, while at high e$^-$ beam dose rate, ca. 10, 000 e/nm^2·s, noticeable changes both in the morphology and in the crystal structure of the nanosheets, as shown in Fig.1 (b-d) and (f-h), can be observed as a function of total beam dose. It was found out that bismuth nanoparticles grew randomly in the matrix of the BiOCl nanosheet, and their numbers and sizes increased quickly with the rise of total e$^-$ beam dose from 2.98×10^7 e/nm^2 to 1.3×10^8 e/nm^2. Eventually, the bismuth nanoparticles with diameters centered at 7.5 nm (average particle size of 9.17 nm) were obtained as shown in Fig. 1 (k), indicating the e$^-$ beam induced transformation over the entire irradiated region. When the BiOCl nanosheet was subjected to e$^-$ beam irradiation with total dose of 1.3×10^8 e/nm^2, the spotted patterns were transformed to ring patterns associated with the randomly orientated bismuth nanoparticles. The three strongest reflections displayed in the SAED can be indexed as (012), (110) and (021) of the rhombohedral (hexagonal axes) bismuth (JCPDF: 85-1331).

Furthermore, it was also noticed that the intensity distribution of the diffraction spots (excluding the direct beam, indicated by a white circle) varied during the e$^-$ beam irradiation. As the intensity distribution of the diffraction spots is strongly dependent on the orientation of a crystalline specimen with the incident beam, it can be hypothesized that the orientation of the BiOCl nanosheet on carbon film is slightly tilted due to the growth of the bismuth nanoparticles.
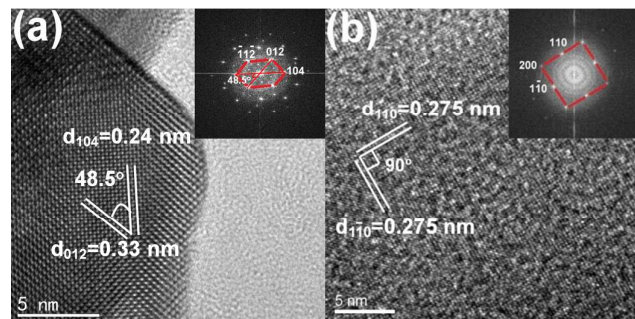
HRTEM characterization

Fig. 2. HRTEM images and the corresponding FFT spectra (insets) of an individual bismuth nanoparticle viewed along the zone axis of [42 1] (a) and an as-prepared BiOCl nanosheet viewed along the zone axis of [001] (b), respectively.

Fig. 2 (a) shows a HRTEM image of an individual bismuth nanoparticle produced by the e$^-$ beam irradiation, and the interplanar spacings of 0.33 and 0.24 nm were measured from two sets of well-defined lattice fringes with an included angle of about

48.5^o as labelled in the HRTEM image. By looking up the table of interplanar spacings, the properties of the measured two lattice planes matched those of the (012) and (104) planes of rhombohedral bismuth crystal, which theoretically have d-spacings of 3.2705 Å and 2.3605 Å, respectively with an included angle of 48.9 ^{o} (on the basis of hexagonal system). Based upon the Weiss zone law, the orientation of the bismuth nanoparticle can be further identified [421] zones axis and the reflection spots in fast Fourier transform (FFT), as shown in the inset in Fig. 2 (a), can be indexed accordingly. The 0.275 nm interplanar spacing of (110) and the 90° angle between (110) and (110), as shown in Fig. 2 (b) for an as-prepared BiOCl nanosheet, are compatible with the theoretical d-spacing and angle values for the generic tetragonal system.
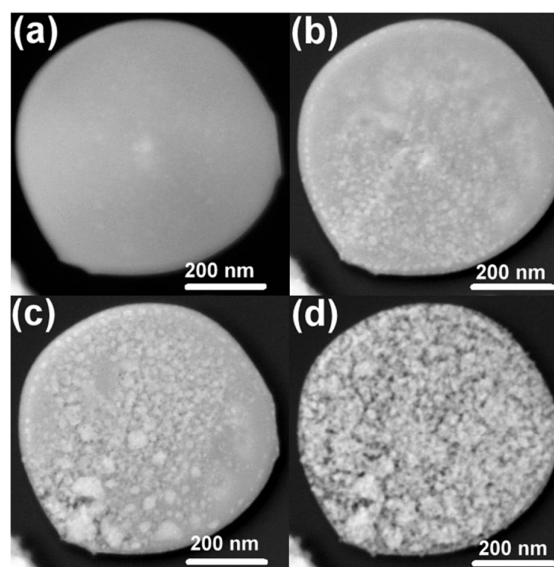
STEM-HAADF characterization

Fig. 3. STEM-HAADF images of a BiOCl nanosheet before (a) and after e$^-$ beam irradiation in TEM mode (electron dose rate: 4.0×10^5 e/nm^2 ·s) for 10 mins (b), 20 mins (c) and 40 mins (d), respectively.

STEM-HAADF images (so called Z-contrast images) are generated by collecting very high angle scattered electrons, and the intensity of these images is monotonically proportional to the atomic number of the specimen.[43] This imaging technique further allows us to observe the mass-thickness evolution of BiOCl along the [001] direction during e$^-$ beam irradiation process. Fig. 3(a) depicts a STEM-HAADF micrograph of an as-prepared BiOCl nanosheet with a diameter of ca. 655 nm. Homogenous image contrast suggests the uniform thickness and single crystallinity in the BiOCl nanosheet. The nanosheet was exposed to the e$^-$ beam irradiation in TEM mode for 10, 20 and 40 mins and the collected images are shown in Fig. 3 (b-d). The higher contrast of randomly produced bismuth nanoparticles in the BiOCl matrix and their increased population were noticed with the prolonged exposure period of the e$^-$ beam, and the nanosheet eventually turned into a porous structure after 40 mins exposure (Fig. 3d) possibly due to the partial decomposition of BiOCl in the presence of the e$^-$ beam. As proved by SAED and TEM analysis, the

resultant nanosheet is no longer a single crystal but is disintegrated into many individual domains (bismuth nanocrystals).

Chemical composition characterization

Variations in chemical composition of samples, caused by the e^- beam exposure, have been extensively reported in in-situ TEM studies. Sepulveda-Guzman et al. reported the in situ formation of bismuth nanoparticles from $NaBiO_3$ induced by e^- beam in TEM. They noticed considerably increase in ratio of bismuth to sodium after reduction of $NaBiO_3$ into bismuth nanoparticles under e^- beam irradiations, possibly due to the segregation of sodium and oxygen or volatilization in vacuum.[27] Su et al. carried out a real-time observation of the reduction of V_2O_5 to V_6O_{13} induced by e^- beam in TEM, which was explained as the loss of oxygen from the top of V-O layer in V_2O_5 crystal as well as the diffusion of oxygen from the bulk phase to the surface. The loss of oxygen atoms at the surface of metal oxides could be attributed to the inter-atomic Auger process.[44] Liu et al. noticed real-time formation of Fe_3O_4 (O) on Fe_4N (γ') in a 400kV TEM for the first time. It was believed that the nitrogen in Fe_4N might be desorbed into the vacuum after the oxidation of Fe_4N induced by the electron beam.[45]
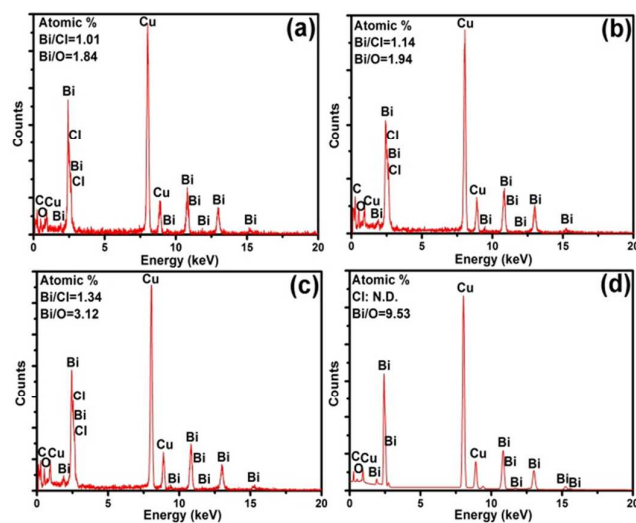

Fig. 4. EDS spectra acquired from the entire BiOCl nanosheet before (a) and after electron irradiation (electron dose rate: 4.0×10^5 e/nm^2 ·s) for 10 mins (b), 20 mins (c) and 40 mins (d). The dose rate of e^- beam during the EDS acquisition process was 120 e/nm^2 ·s.

Fig. 4 depicts the acquired EDS spectra of BiOCl specimens under identical e^- beam irradiation dose for different periods. Under low dose of e^- beam irradiation, bismuth, oxygen and chloride EDS signals were apparently noticed, and the semi-quantitative molar ratio of Bi/O/Cl was 1/0.54/0.99. The non-stoichiometric molar ratio between bismuth and oxygen could be attributed to the oxygen vacancies produced by e^- beam exposure.[21] Considerable increase in molar ratios of both Bi/Cl and Bi/O were found with the continuous exposure of beam irradiations. After 40 mins of beam exposure, chloride was not detected and the molar ratio of Bi/O eventually reached to 9.53, as shown in Fig. 4 (d), suggesting the newly formed nanocrystals are chloride free and only contain bismuth and oxygen.

Effect of supporting film

Previous studies showed that carbon materials can be activated under e^- beam in certain circumstances via direct atomic displacement or activation and radiolysis.[46] Consequently, carbon materials may have reducing property in the presence of e^- beam with sufficient energy. To completely rule out the possibility of the reduction process being affected by the carbon film on copper grid, the growth of bismuth nanoparticles was attempted on formvar film coated grid. As depicted in Fig. S1 (ESI), the selected BiOCl is single crystalline and exposing {001} facets only. It appears that the formation and growth of Bi nanoparticles proceed in a nearly identical manner to that observed for the carbon film experiment. Many particles were observed having (001) planes of BiOCl after e^- beam irradiation for 30 mins. In the meantime, the ring-like SAED patterns, which can be indexed as the reflections of rhombohedral bismuth, were noticed, indicating partially transformation of BiOCl under e^- beam. Hence the formation and growth of bismuth nanoparticles on BiOCl is arguably not to the ascription of the carbon supported film, but rather the influence of e^- beam.

Mechanism discussion

Generally, the e^- beam induced transformation includes one or combination of three principal mechanisms: inelastic scattering breaks the chemical bonds (radiolysis); direct displacement of atoms from the crystal lattice creates point defects (knock-on process); and the heating effect caused by the phonons.[47] The BiOCl crystals are thermostable up to 500 ^{o}C.[48] The melting points of bulk and nanoscaled (10 nm in diameter) bismuth are ca. 271 ^{o}C and 180 ^{o}C, respectively.[49] The realistic temperature on the specimen inside a TEM is normally less than 100 ^{o}C.[50] Hence the heating effect from the e^- beam on the growth of bismuth nanoparticles can be ignored.
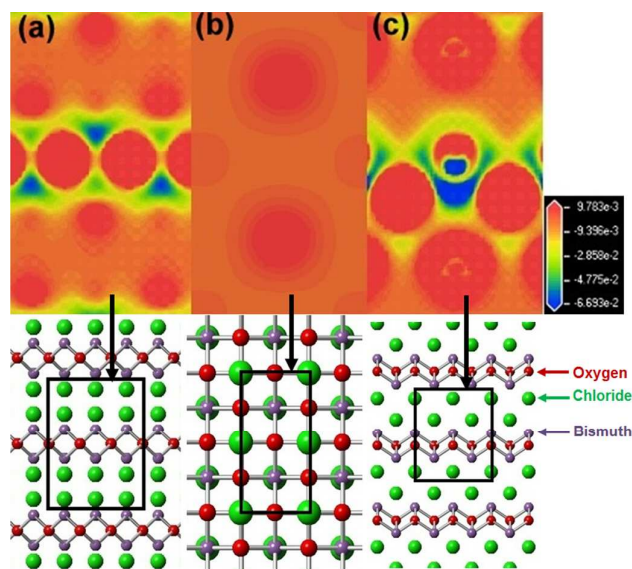

Fig. 5 Electron density maps and the corresponding atomic locations (bismuth, oxygen and chloride atoms are purple, red and green balls, respectively) in BiOCl crystal along the exposed facets of {110} (a), {001} (b) and {010} (c), respectively.

ARTICLE

Fig. 5 depicts the electron density maps for the BiOCl crystals viewed along the direction of [110], [001] and [010], respectively. The relative higher electron density was noticed in [Bi_2O_2] slabs along the [001] direction of BiOCl as shown in Fig. 5 (b), possibly due to the influence by the neighbour oxygen and chloride atoms with high electronegativity. The contour plots reveal that the bonding between Bi and O exhibits a covalent nature, which is due to the hybridization of O_{2p} and Bi_{6p} orbitals. The most positively charged area was found in the interlamellar space between (001) lattice planes (viewed along the direction of [110] and [010]). In our case, the positively charged area in the exposed {001} facets would be attacked by e$^-$ beam with high priority,[29] and a charge-up process where electrons tend to gather at the surface of BiOCl might be expected as the prerequisite for the formation of bismuth over BiOCl through radiolysis mechanism.
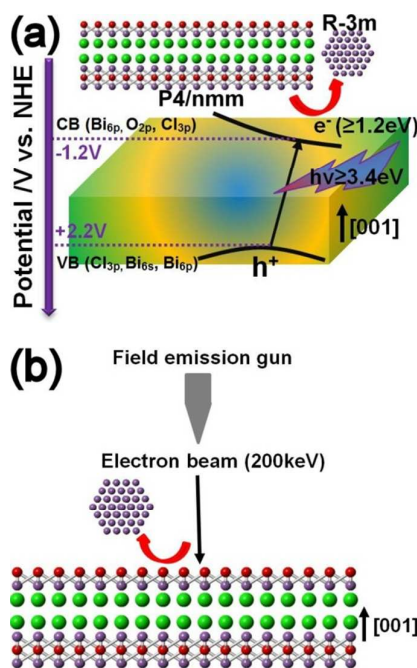

Fig. 6 Schematic illustration of the comparison between bismuth nanostructures growth on BiOCl driven by UV photon (a) and e$^-$ beam (b).

When e$^-$ beam hit vertically at the entire sample area, parts of electrons experienced inelastic scattering and transfer certain energy to the sample. Therefore, the inter and intra band transitions as well as other effects such as phonon excitations and plasmon excitations can be expected, which are considered as the classical process of energy loss.[51] BiOCl is an indirect semiconductor with a band gap energy of 3.4 eV, and the corresponding conduction and valence band (CB and VB) edges are reported at -1.2 V and 2.2 V (vs. NHE), respectively.[21,24] If the energy transferred from inelastically scattered electrons is equal to or greater than 3.4 eV, a pair of electron and hole will be generated at CB and VB, respectively. Because Bi_{6p} make a major contribution above the Fermi level and the potential of the CB bottom is -1.2 V,[52] the energy of photogenerated electron at CB will be equal to or even greater than 1.2 eV, which is sufficient to reduce Bi(III) into bismuth ($BiOCl+2H^++3e^- \rightarrow Bi+Cl^-+H_2O$, E^0=0.1583V vs. SHE[53]). In the

course of radiolysis, the chloride anions (Cl_{3p} contributes both CB and VB[52]) displaced by high energy electrons may shrink to dislocation loops and finally diffuse to the surface of BiOCl, leading to the loss of chloride anions, which favour the formation of metallic bonds in elementary bismuth.[54] Then afterwards bismuth clusters, crystal nuclei, nanoparticles and finally the larger single crystals successively grew on the BiOCl nanosheets.[55] On the other hand, it is also necessary to take account of direct reduction of Bi(III) in BiOCl by high energy e$^-$ beam, which has been adopted and proved as a reducing agent in the growth of metallic nanoparticles in liquid TEM stage.[33] Thus, it is reasonable to believe that the UV-induced photoreduction of bismuth nanoparticles on BiOCl photocatalyst[24] resembles with the formation of nanostructured bismuth onto BiOCl nanosheets driven by e$^-$ beam and their processes are schematically illustrated in Fig. 6. In the photoreduction synthesis of Bi/BiOCl composites, continuous photogenerated electrons, which are regarded as an "e$^-$ beam", can be created in BiOCl photocatalyst under persistent UV light irradiation regardless of others processes that inhibit the photoreduction performance such as the recombination of carries and trapping of electrons by grain boundaries, etc.
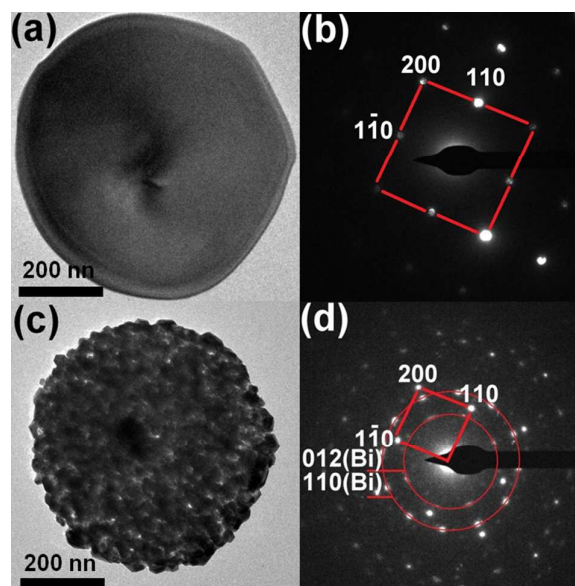

Fig. 7 80kV TEM images and the corresponding SAED patterns of a BiOCl nanosheet before (a, b) and after e$^-$ beam irradiation (dose rate: 9.5×10^4 e/nm^2·s) for 15 mins (c, d).

If knock-on displacement, the high energy e$^-$ beam displace atomic nuclei to interstitial positions and degrade the crystalline perfection, is the main mechanism, it would be reasonable to believe that the formation of bismuth will be greatly inhibited by decreasing the accelerating voltage substantially.[54, 56] To confirm the assumed possible knock-on effect, low-voltage TEM observation was performed in another set of experiments. As shown in Fig. 7, a single BiOCl nanosheet exposed under an 80 kV e$^-$ beam with a similar dose rate of 9.5×10^4 e/nm s for 15 mins, but no suppression in the growth of the bismuth nanoparticles was noticed, further confirming the major contribution of radiolysis mechanism in the transformation process. But the knock-on effect still cannot be

completely ignored due to the extremely high momentum of the incident electrons. In the case of 200 kV accelerating voltage, the maximum calculated transferred-energies from a relativistic electron that knocks a nucleus directly are 2.544 eV, 33.232 eV and 14.997 eV for bismuth, oxygen and chloride atoms, respectively.[28, 57] Unfortunately, the threshold displacement energies (E_d) for bismuth and chloride containing compounds are rarely reported, and the reported E_d values for oxygen vary from 20 to 60 eV due to strong dependence on the types of bonding status as well as the crystallographic orientation.[58-61] But it is understandable that compared with the bismuth, displacements of oxygen and chloride atoms might preferentially take place due to the relatively higher transferred energies.
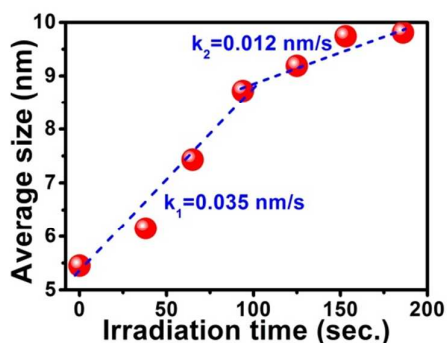
Coalescence of bismuth nanoparticles

Fig.8 Evolution of the average particle size as a function of e⁻ beam irradiation time.

As being continuously irradiated under the e⁻ beam, the nucleation of bismuth occurs in a fraction of second that gives way to the growth and coalescence, which have been directly observed in real time. Changes in average particle size of the bismuth nanoparticles as a function of the irradiation time were investigated within the field of view (Fig. S2, ESI). Fig. 8 shows that the average particle size reached to 9.74 nm after the e⁻ beam irradiations for 153 seconds. However, further increase in the irradiation time was not found beneficial for the growth of the nanoparticle size, and only slight increase in the average size was achieved in the next 33 seconds irradiations. Smaller nanoparticles tend to promptly coalesce to the neighbouring nanoparticles so that the speed of the growth which was faster at the early stage till 94 seconds is 0.035 nm s⁻¹. The density decline of the nanoparticles caused by the growing up of these nanoparticles may decrease their collision possibilities,[62] and hence slow the growing speed down to 0.012 nm s⁻¹ at the later stage of the growth (94-186s). In addition, an increasing number of Moiré fringes were observed in a time-series of TEM images, as depicted in Fig. S2, due to the stacking behaviour of bismuth nanoparticles along the thickness.
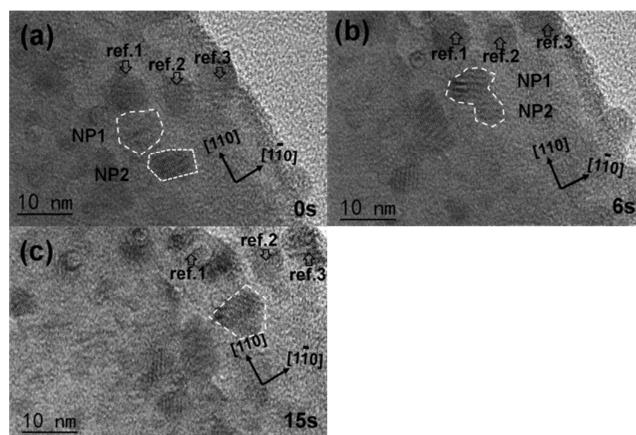

Fig. 9 Time series of HRTEM images (viewed along the [001] direction of BiOCl) showing the coalescence of two nanoparticles (NP1&2, dose rate: 4.5 ×10⁵ e/nm²·s). Three reference points are labelled with "ref. 1, 2 and 3". The lapse time has been rounded to the nearest integer seconds.

It is likely that bismuth nanoparticles have similar formation course, however, they have growth along different pathways. Fig. 9 illustrates a few selected sequentially recorded TEM images at the most instructive time steps that display the asymmetric coalescence of two unequal sized bismuth nanoparticles as e⁻ beam irradiation proceeds. At the early stage, as shown in Fig. 9 (a), smaller nanoparticle (NP2) with size of 7.33 nm migrated towards the bigger one (NP1) having size of 8.78 nm due to the dipole-dipole electrostatic interaction.[63] In the subsequent stage, both the nanoparticles were merged by coalescence and a "neck" with diameter of 3.24 nm was observed which is depicted in Fig. 9 (b). Eventually the dumbbell like nanoparticle relaxed into a spherical particle having size of 9.72 nm, as shown in Fig. 9(c), under the driving force of minimizing the number of dangling bonds via decreasing the surface area.[64]
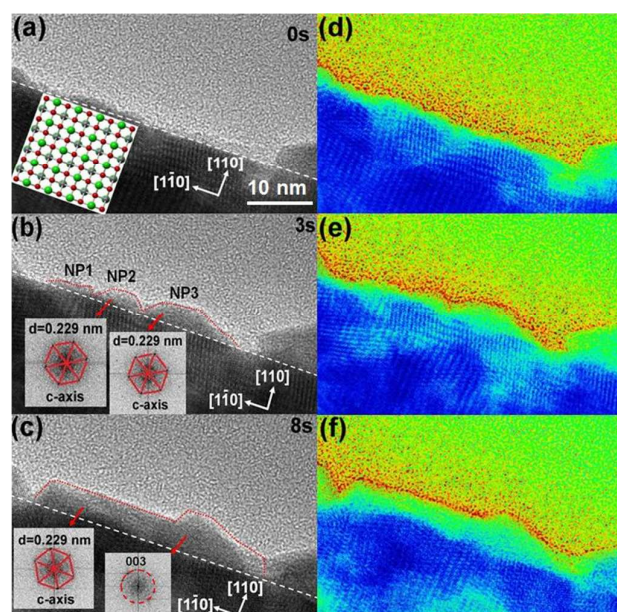
ARTICLE

Fig. 10 Snapshots of HRTEM images (a-c, viewed along the [001] direction of BiOCl) showing the coalescence of three nanoparticles (NP1-3, dose rate: 8.9 ×10^{5} e/nm[2]·s), and the corresponding colour gradient maps displaying the coalescence behaviour (d-f). The inset of (a) depicts the crystal structure of BiOCl with (001) orientation (bismuth, oxygen and chloride atoms are purple, red and green balls, respectively). The insets of (b, c) show the of FFT patterns of selected areas. The displayed time has been rounded to the nearest integer seconds.

Fig. 10 displays a different type of coalescence event of multiple nanoparticles. At first, single crystalline bismuth nanoparticles orientated to the *c*-axis were formed on the (110) facet of BiOCl, and then sequential coalescence events took place in the presence of e[-] beam; finally, the elongated polycrystalline nanoparticles with nanorod liked morphology (43.4 nm in length and 5.2 nm in width) were resulted. The final shape of the nanoparticles after crystal growth is usually decided by the competition between coalescence and collision processes. Larger spherical particles will be produced if the coalescence time is less than collision time. The coalescence of nanoparticles have specifically been evidenced in liquid cell based in situ TEM monitoring system[33, 62, 63] because of the relatively low concentration of nanoparticles in the cell, while a collection of smaller attached particles (i.e. the aggregates) will be resulted if the coalescence is negligibly slower than collision process.[62, 64]

It is believed that the morphological evolution of bismuth in the formation of Bi/BiOCl composite photocatalyst should be essential to the light harvesting properties of bismuth because of the LSPR effect. The UV-Vis absorption spectra also reveal that the hybridization of bismuth on BiOCl semiconductor gives rise to the continuous absorption of visible light from 380-780 nm, which might be attributed to the LSPR effect of nanostructured bismuth (Fig. S3, ESI). It is inferred that the LSPR energy gap of bismuth nanoparticles should be less than 1.6 eV, assuming the absorption band centered at 780 nm. But, of more interest to us, is the electron energy-loss spectroscopy (EELS) which has been demonstrated as a very powerful tool for identifying the SPR behaviour of various nanostructures.[65, 66] Therefore, during the crystal growth process, the LSPR peak of bismuth nanoparticles could be measured in real time by means of a high energy resolved EELS equipped with monochromator, which remains undiscovered and is currently under investigation in our lab. Thus a direct correlation between the light harvesting ability and the catalyst growth kinetics could be anticipated, which would eventually guide the synthesis of highly-efficient bismuth based composite photocatalyst.

Conclusions

In summary, the growth and coalescence of bismuth nanoparticles on 2D structured BiOCl photocatalysts was studied under e[-] beam exposure via an in situ TEM characterization technique. Investigations using first-principle calculation of the electron density maps for BiOCl and the low-voltage electron microscopy (at 80kV) suggested that the effects of both radiolysis and knock-on simultaneously play a role in the formation process of the bismuth nanoparticles. The asymmetric coalescence of unequal sized

nanoparticles as well as the coalescence of multiple nanoparticles was observed during the growth of the bismuth nanoparticles.

This work not only directly reveals the formation and growth of bismuth nanoparticles on BiOCl nanosheets in real time via the in situ TEM characterization technique, but also sheds light on the resemblance of growth behaviours between the UV and e[-] beam induced growth of bismuth nanoparticles on BiOCl photocatalysts, which could provide a better understanding of the synthetic chemistry of bismuth based composite photocatalysts.

Acknowledgements

Notes and references

‡ These authors contribute equally to this work.

References

1 A. Fujishima and K. Honda, *Nature,* 1972, **238**, 37.

2 M. R. Hoffmann, S. T. Martin, W. Y. Choi and D. W. Bahnemann, *Chem. Rev.,* 1995, **95**, 69

3 A. Kudo and Y. Misekia, *Chem. Soc. Rev.,* 2009, **38**, 253.

4 Q. Fu, Encyclopedia of Atmospheric Sciences (Edited by J. Holton, J. Pyle, and J. Curry), Academic Press, 2002, 1859.

5 Z. Zou, J. Ye, K. Sayama and H. Arakawa, *Nature,* 2001, **414**, 625.

6 R. Asahi, T. Morikawa, T. Ohwaki, K. Aoki and Y. Taga, *Science,* 2001, **293**, 269.

7 X. B. Chen, L. Liu, P. Y. Yu and S. S. Mao, *Science,* 2011, **331**, 746.

8. Z. J. Han, F. Qiu, R. Eisenberg, P. L. Holland and T. D. Krauss, *Science,* 2012, 338, 1321.

9 D. M. Schultz and T. P. Yoon, *Science,* 2014, **343**, 985.

10 J. Liu, Y. Liu, N. Y. Liu, Y. Z. Han, X. Zhang, H. Huang, Y. Lifshitz, S. T. Lee, J. Zhong and Z. K. Kang, *Science,* 2015, **347**, 970.

11 K. Awazu, M. Fujimaki, C. Rockstuhl, J. Tominaga, H. Murakami and T. Watanabe, *J. Am. Chem. Soc.,* 2008, **130**, 1676.

12 S. Linic, P. Christopher and D. B. Ingram, *Nature,* 2011, **10**, 911.

13 H. X. Lin, L. Y. Ding, Z. X. Pei, Y. G. Zhou, J. L. Long, W. H. Deng and X. X. Wang, *Appl. Catal. B: Environ.,* 2014, **160-161**, 98.

14 H. M. Chiu, T. H. Yang, Y. C. Hsueh, T. P. Perng and J. M. Wu, *Appl. Catal. B: Environ.,* 2015, **163**, 156.

15 W. Zhao, Y. Guo, S. M. Wang, H. He, C. Sun and S. G. Yang, *Appl. Catal. B: Environ.,* 2015, **165**, 335.

16 J. Toudert, R. Serna and D. C. Jiménez, *M. J. Phys. Chem. C,* 2012, **116**, 20530.

17 J. M. McMahon, G. C. Schatz and S. K. Gray, *Chem. Chem. Phys.,* 2013, **15**, 5415.

18 Z. Wang, C. L. Jiang, R. Huang, H. Peng and X. D. Tang, *J. Phys. Chem. C,* 2014, **118**, 1155.

19 F. L. Xia, X. Y. Xu, X. C. Li, L. Zhang, L. Zhang, H. X. Qiu, W. Wang, Y. Liu and J. P. Gao, *Ind. Eng. Chem. Res.,* 2014, **53**, 10576.

20 F. Dong, Q. Y. Li, Y. J. Sun and W. K. Ho, *ACS Catal.,* 2014, **4**, 4341.

21 Y. Yu, C.Y. Cao, H. Liu, P. Li, F. F. Wei, Y. Jiang and W. G. Song, *J. Mater. Chem. A,* 2014, **2**, 1677.

22 X. M. Zhang, G. B. Ji, Y. S. Liu, X. G. Zhou, Y. Zhu, D. N. Shi, P. Zhang, X. Z. Cao and B. Y. Wang, *Phys. Chem. Chem. Phys.,* 2015, **17**, 8078.

23 S. X. Weng, B. B. Chen, L. Y. Xie, Z. Y. Zheng and P. Liu, *J. Mater. Chem. A,* 2013, **1**, 3068.

24 J. J. Hu, G. Q. Xu, J. W. Wang, J. Lv, X. Y. Zhang, Z. X. Zheng, T. Xie and Y. C. Wu, *New J. Chem.,* 2014, **38**, 4913.

25 H. Zhang, Y. Ma, F. J. Quan, J. J. Huang, F. L. Jia and L. Z. Zhang, *Electrochem. Commun.,* 2014, **46**, 63.

26 S. H. Kim, Y. S. Choi, K. Kang, S. I. Yang. *J. Alloy Compd.,* 2007, **427**, 330.

27 S. Sepulveda-Guzman, N. E. Villarreal, D. Ferrer, A. T. Castro, X. Gao, J. P. Zhou and M. J. Yacaman, *Nanotechnology,* 2007, **18**, 335604.

28 J. Ghatak, W. Guan and G. Möbus, *Nanoscale,* 2012, **4**, 1754.

29 E. Longo, L. S. Cavalcante, D. P. Volanti, A. F. Gouveia, V. M. Longo, J. A. Varela, M. O. Orlandi and J. Andrés, *Sci. Rep.,* 2013, **3**, 1676.

30 W.D. Pereira, J. Andres, L. Gracia, M.A. San-Miguel, E.Z. da Silva, E. Longo and V.M. Longo, *Phys. Chem. Chem. Phys.,* 2015, **17**, 5352.

31 H. M. Zheng, J. B. Rivest, T. A. Miller, B. Sadtler, A. Lindenberg, M. F. Toney, L. W. Wang, C. Kisielowski and A.P. Alivisatos, *Science,* 2011, **333**, 206.

32 H. G. Liao, Cui, S. Whitelam and H. M. Zheng, *Science,* 2012, **336**, 1011.

33 H. G. Liao, D. Zherebetskyy, H. L. Xin, C. Czarnik, P. Ercius, H. Elmlund, M. Pan, L. W. Wang and H. M. Zheng, *Science,* 2014, **345**, 916.

34 X. F. Chang, S. B. Wang, Q. Qi, M. A. Gondal, S. G. Rashid, D. Y. Yang, M. A. Dastageer, K. Shen, Q. Y. Xu and P. Wang, *Appl. Catal. B: Environ.,* 2015, **176**, 201.

35 M. C. Payne, M. P. Teter, D. C. Allan, T. A. Arias and J. D. Joannopoulos, *Rev. Mod. Phys.,* 1992, **64**, 1045.

36 M. D. Segall, P. J. D. Lindan, M. J. Probert, C. J. Pickard, P. J. Hasnip, S. J. Clark and M. C. Payne, *J. Phys.: Condens. Matter,* 2002, 14, 2717.

37 D. Vanderbilt, *Phys. Rev. B,* 1990, **41**, 7892-7895.

38 J. P. Perdew, K. Burke and Y. Wang, *Phys. Rev. B,* 1996, **54**, 16533.

39 J. P. Perdew, K. Burke and M. Ernzerhof, *Phys. Rev. Lett.,* 1996, **77**, 3865.

40 H. J. Monkhorst and H. D. Pack, *Phys. Rev. B,* 1976, **13**, 5188.

41 T. H. Fischer and J. Almlof, *J. Phys. Chem.,* 1992, **96**, 9768.

42 G. Kresse and Furthmuller, *J. Phys. Rev. B,* 1996, **54**, 11169.

43 S. J. Pennycook, D. E. Jesson, A. J. McGibbon and P. D. Nellist, *J. Electron. Microsc.,* 1996, **45**, 36.

44 D. S. Su, M. Wieske, E. Beckmann, A. Blume, G. Mestl and R. Schlögl, *Catal. Lett.,* 2001, **75**, 81.

45 Z. Q. Liu, H. Hashimoto, E. Sukedai, M. Song, K. Mitsuishi and K. Furuya, *Phys. Rev. Lett.,* 2003, **90**, 255504.

46 P. S. Spinney, D. G. Howitt, S. D. Collins and R. L. Smith, *Nanotechnology,* 2009, **20**, 465301.

47 D. B. Williams and C. B. Carter, Transmission Electron Microscopy: A Textbook for Materials Science (2nd edition), Springer publisher, 2009.

48 Z. T. Deng, F. F. Tang and A. J. Muscat, *Nanotechnology,* 2008, **19**, 295705.

49 K.Y. Niu, J. Park, H.M. Zheng and A. P. Alivisatos, *Nano Lett.,* 2013, **13**, 5715.

50 B. S. Xu and S. I. Tanaka, *Supramol. Sci.,* 1998, **5**, 227.

51 R. F. Egerton, *Rep. Prog. Phys.,* 2009, **72**, 016502.

52 K. L. Zhang, C. M. Liu, F. Q. Huang, C. Zheng and W. D. Wang, *Appl. Catal. B: Environ.,* 2006, **68**, 125.

53 D. R. Lide, CRC Handbook of Chemistry and Physics, 87th edition, 2006-2007.

54 R. F. Egerton, P. Li and M. Malac, *Micron,* 2004, **35**, 399.

55 D. Golberg, M. Mitome, L. W. Yin and Y. Bando, *Chem. Phys. Lett.,* 2005, **416**, 321.

56 R. F. Egerton, *Microsc. Res. Techniq.,* 2012, **75**, 1550.

57 R. F. Egerton, P. A. Crozier and P. Rice, *Ultramicroscopy,* 1987, **23**, 305.

58 P. Bois and F. Beuneu, *J. Phys. F: Met. Phys.,* 1987, **17**, 2365.

59 C. Meis and A. Chartier, *J. Nucl. Mater.,* 2005, **341**, 25.

60 P. A. F. P. Moreira, R. Devanathan, J. G. Yu and W. J. Weber, *Nucl. Instrum. Meth. B,* 2009, **267**, 3431.

61 K. L. Smith, M. Colella, R. Cooper and E. R. Vance, *J. Nucl. Mater.,* 2003, **321**, 19.

62 K. Y. Niu, H. G. Liao and H. M. Zheng, *Microsc. Microanal.,* 2014, **20**, 416.

63 H. L. Xin and H. M. Zheng, *Nano. Lett.,* 2012, **12**, 1470.

64 T. Hawa and M. R. Zachariah, *Aerosol Sci.,* 2006, **37**, 1.

65 M. H. Gass, U. Bangert, A.L. Bleloch, P. Wang, R.R. Nair and A.K. Geim, *Nat. Nanotechnol.,* 2008, **3**, 676.

66 C. K. Xu, W. J. Liu, P. K. Zhang, M. Li, H. J. Zhang, K. Z. Xu, Y. Luo and X. Jun, *Nat. Phys.,* 2014, **10**, 753.

Dalton Transactions Accepted Manuscript